



Study on the influence of region of interest on the detection of total sugar content in apple using hyperspectral imaging technology

Xueting MA^{1,2} , Huaping LUO^{1,2,*}, Fei ZHANG^{1,2}, Feng GAO^{1,2}

Abstract

This paper explores the influence of the selection method of the region of interest (ROI) on the results in the total sugar of apple detection based on hyperspectral imaging technology. Taking Fuji apple as the detection object, the hyperspectral images of the samples were collected based on the 900~1750 nm hyperspectral imaging system, and the total sugar content of the samples was obtained based on the anthrone colorimetric method. The square ROI and circular ROI of different sizes were extracted. The average spectrum of the region was used to establish a quantitative analysis model of apple's total sugar content by partial least squares (PLS). The results show that apple's total sugar detection model established by extracting a circular ROI with a diameter of 25 pixels has the highest accuracy and strongest prediction ability ($R_c = 0.8977$, RMSEC = 0.6459, $R_p = 0.8836$, RMSEP = 0.6627). The research shows that selecting ROI with a suitable shape and size for the research object is of great significance for improving the accuracy of the prediction model of apple's total sugar content and giving play to the advantages of hyperspectral images.

Keywords: hyperspectral imaging technology; ROI; PLS; Fuji apple; total sugar content.

Practical Application: Most scholars focus on the study of signal preprocessing and the algorithms involved in modeling when building fruit quality prediction models based on hyperspectral imaging technology. The selection of regions of interest in hyperspectral images is directly related to the quality of data sources. In this paper, the influence on the prediction model of apple total sugar content is explored by selecting regions of interest with different sizes of square and circular, to provide some technical support for the research in this field.

1 Introduction

Hyperspectral imaging technology integrates advanced technologies in the fields of optics, optoelectronics, information processing and computer (Zou et al., 2022), integrates image processing and spectral analysis, realizes the simultaneous acquisition of object spatial information and spectral information (Chen et al., 2022), and can detect the appearance characteristics and internal components of the object to be tested at the same time (Duan et al., 2022; Sulaiman et al., 2022). The hyperspectral images obtained based on imaging spectrometers have nanometer spectral resolution, covering the spectral range from ultraviolet to long-wave infrared (200~14000 nm), and continuously image at hundreds of wavelengths (Bai et al., 2022; Sun et al., 2021).

Because hyperspectral remote sensing can provide a large amount of characteristic spectral information, it has been widely used in the fields of surface material identification (Li et al., 2022b; Ye et al., 2021), water quality detection (Cao et al., 2022; Liu et al., 2021), and vegetation coverage detection (Egorov & Kozoderov, 2021; Miller et al., 2022; Pi et al., 2021), and a series of research findings have been obtained. In recent years, hyperspectral imaging technology has been gradually applied to qualitative and quantitative research on fruit quality. Fu & Wang (2022) used fluorescence hyperspectral imaging technology to detect the surface scratch of pears. A qualitative analysis model was established based on a support vector machine and random forest machine learning method to distinguish the

scratch degree and scratch time of samples. The results showed that different degrees of scratches could be recognized after 15 minutes of scratching, with an accuracy of 93.33%. Xu et al. (2022) used hyperspectral imaging technology to carry out non-destructive detection of total soluble solids (TSS) in grapes. They proposed a new method (VMD-RC) including variational mode decomposition and regression coefficient to select characteristic wavelengths, and established prediction models of TSS based on least squares support vector machine (LSSVM) and partial least squares (PLS). The results show that VMD-RC algorithm can be used to process high-dimensional hyperspectral image data, and HSI has great potential in the nondestructive and rapid evaluation of fruit quality attributes. Yuan et al. (2021) obtained data based on hyperspectral imaging technology, and established a jujube damage discrimination model based on PLS-DA, linear discriminant analysis (LDA) and support vector machine (SVM), respectively. The results show that PLS-DA is the best discriminant model, which can effectively detect the damage of jujube with time.

Existing related papers mostly focus on spectral data or image preprocessing and model building, and less on how to extract ROI. The selection of ROI in the hyperspectral image is the selection of the source data, which will directly affect the accuracy and stability of the qualitative or quantitative analysis model. In this study, the total sugar contents of Fuji apples were

Received 29 July, 2022

Accepted 02 Sept., 2022

¹Modern Agricultural Engineering Key Laboratory at Universities of Education, Department of Xinjiang Uyghur Autonomous Region, Tarim University, Alar, China

²College of Mechanical and Electrical Engineering, Tarim University, Alar, China

*Corresponding author: 120160004@taru.edu.cn

selected as the target of nondestructive testing, and a quantitative analysis model was established based on hyperspectral imaging technology. The average spectra of the square and circular ROI with different sizes were extracted, and the PLS was used to establish a quantitative analysis model for the total sugar content of apples, and the influence of the shape and size of ROI on the model was analyzed, to provide theoretical and technical support for the extraction of ROI in apple's total sugar content detection.

2 Materials and methods

2.1 Apple samples preparation

The experiment selected Fuji apples as the research object, and the samples were picked from the apple orchard of Hongqipo Farm in Aksu City, Xinjiang, China. A total of 60 apples with ideal shape, uniform size, and no defects or contamination were selected, and the fruit diameter was 75–80 mm. The samples were numbered and stored in a 4 °C freezer. Before the test, the apples were taken out of the freezer and placed in the laboratory for 12 hours, so that the overall temperature of the apple samples was consistent with the ambient temperature, and moisture on the surface of the apples was prevented from affecting the collection of hyperspectral images. The laboratory temperature during the test was about 25 °C, and the relative humidity was about 55%.

2.2 Hyperspectral imaging system

As shown in Figure 1, the hyperspectral image data of apple samples were obtained by a spectrometer-based hyperspectral image acquisition system. The system is mainly composed of a spectral camera (Image-N17E-N3, Sichuan Shuangli Hepu Technology Co., Ltd.) and a push-broom hyperspectral sorting system (Hyperspectral Sorting System push-broom hyperspectral sorting system of Beijing Zhuoli Hanguang Co., Ltd.). The spectral image acquisition system has an effective spectral range of 900–1750 nm, with 256 bands and 5 nm spectral resolution. The height of the camera is set at 45 cm, with an effective pixel of 320×256 and an exposure time of 11.5 ms. In the test, the moving speed of the transmission belt was set to 2.0 m/min.

2.3 Hyperspectral image acquisition and calibration

In the process of hyperspectral image acquisition, the image will be mixed with some noise information, due to the difference in the intensity distribution of light source in each band and the influence of camera dark current noise (Li et al., 2022a). These noise information will affect the quality of hyperspectral images, and then affect the accuracy and stability of qualitative or quantitative analysis models based on hyperspectral images. Therefore, it is necessary to correct the hyperspectral image to eliminate the influence of noise. The black-and-white correction method is often adopted in the study, and Equation 1 is used for correction, where R_b is the all-black reference hyperspectral image acquired when the light source is turned off and the lens cover is not opened, and R_w is the all-white reference hyperspectral image acquired from the polytetrafluoroethylene standard white plate. HSIA-CT-150 \times 150 standard whiteboard was used in this study for spectral correction. The corrected image can

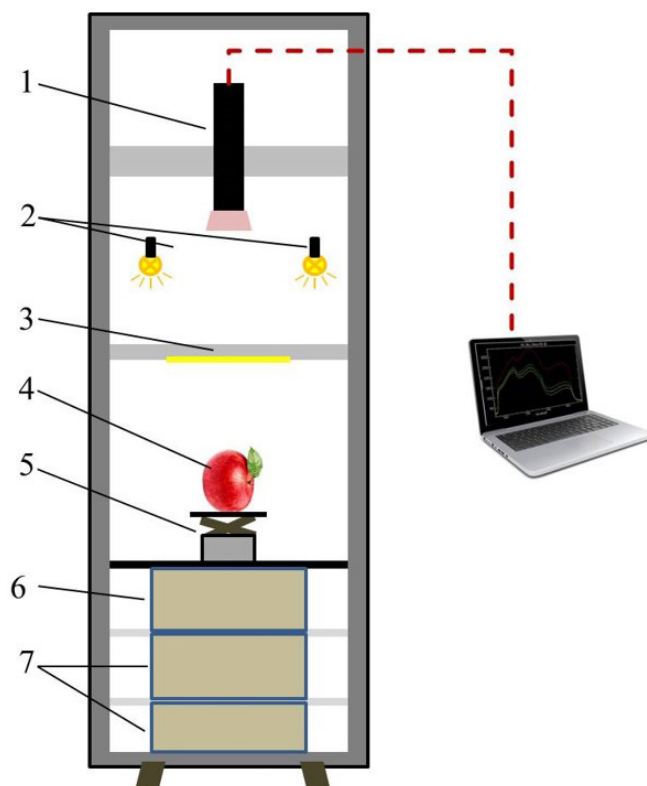


Figure 1. Schematic diagram of the hyperspectral imaging acquisition system. (1) Spectral camera; (2) Light source; (3) Light line; (4) Sample; (5) X-Z stage; (6) X stage controller; (7) Power supply.

be obtained by calculation according to the following formula (Equation 1) (Wang et al., 2022).

$$R = \frac{R_0 - R_b}{R_w - R_b} \quad (1)$$

Where, R is the relative reflectance of the corrected hyperspectral image, %; R_0 is the original apple hyperspectral image; R_b is the blackboard calibration image; R_w is the whiteboard calibration image.

2.4 Region of interest selection

Extracting characteristic spectra is an important part of sample quality detection and analysis based on hyperspectral imaging technology. The shape and size of ROI will affect the subsequent spectral preprocessing, feature selection, modeling analysis and prediction accuracy. In the study, the selection of ROI is centered on the upper spatial vertex when the apple is laid flat, and the average spectra of circular and square ROI with different sizes are extracted. Where the size of the square ROI is sequentially set to 5×5 , 10×10 , 15×15 , 20×20 and 25×25 (unit: pixel, represented by D5, D10, D15, D20 and D25 respectively), and the diameter of the circular ROI is set to 5, 10, 15, 20 and 25 (unit: pixel, represented by D5, D10, D15, D20 and D25 respectively). The spectral data of different ROI were obtained, and the PLS was used to establish the quantitative analysis model of apple's total sugar content, to analyze the influence of the shape and size of ROI on the model results.

2.5 Determination of total sugar in Fuji apples

The determination of total sugar usually includes titration (Chang et al., 2022), spectrophotometry (Paunović et al., 2020), and high-performance liquid chromatography (Armoogum & Boodhoo, 2020; Saafi et al., 2022). The total sugar content of apples in this study was determined by spectrophotometry based on anthrone colorimetry (Zhou et al., 2022).

Detection principle

Sugars can be dehydrated by concentrated sulfuric acid at a high temperature to form furfural or hydroxymethyl sugar aldehyde, and then dehydrated and condensed with anthrone ($C_{14}H_{10}O$) to form furfural derivatives, which are blue-green. The material has a maximum absorption at 620 nm. Within the range of 150 $\mu\text{g/mL}$, the color depth is directly proportional to the soluble sugar content, so it can be used for the detection of total sugar in combination with spectrophotometry (Mu et al., 2021).

Detection process

The total sugar content detection process of Fuji apple is as follows:

- (1) Drawing of glucose standard curve. Take 7 large test tubes and prepare a series of glucose solutions with different concentrations (1 mL) according to the data in Table 1, and put them into the ice water bath for cooling, and take out the seven test tubes from the ice water bath after 5 minutes; add 4.0 mL of anthrone reagent to each test tube, then put seven test tubes into boiling water bath (cover the tube mouth with glass balls to prevent evaporation), take them out after 10 minutes and continue to cool them with running water for 10 minutes; take 2 mL solution from the seven test tubes and add it to the cuvette, and put the seven cuvettes into the photometer to obtain the absorbance value of the solution in each test tube. The standard curve is made with the standard glucose content as the abscissa and the absorbance value as the ordinate.
- (2) Extraction of the total sugar content of Fuji apple. After collecting the hyperspectral images of Fuji apples, prepare 1 g apple flesh and 3 mL distilled water, and put them into a mortar and grind it into a homogenate, and then transfer it into a triangular flask with 25 mL boiling water; take out

the triangular flask and filter it after 30 minutes boiling water bath, and transfer the filtrate into a 50 mL volumetric flask; add an appropriate amount of distilled water to the precipitate in the triangular flask and conduct boiling water bath again for 30 minutes, take it out and filter it, transfer the filtrate into the above 100 mL volumetric flask, and repeat the operation twice; continue to add distilled water to the volumetric flask and dilute it to 100 mL.

- (3) Determination of total sugar content in Fuji apple. Suck 1 mL solution and inject it into the test tube, and put it into the ice water bath for 5 minutes; take out the test tube from the ice water bath after 5 minutes, and add 4 mL anthrone reagent (0.2 g anthrone dissolved in 100 mL concentrated sulfuric acid), and put it into the boiling water bath for 10 minutes after shaking it evenly; cool it with tap water for 10 minutes after taking it out of the boiling water bath, then take 2 mL sample solution from the test tube and inject it into the cuvette (set three parallel samples), and put it into the photometer to obtain the absorbance value of the solution in each cuvette with the wavelength of 620 nm.

The total sugar content of the sample is obtained from formula (Equation 2):

$$S = \frac{C \cdot D}{W \times 10^6} \times 100\%, D = \frac{V_T}{V_S} \quad (2)$$

Where S is the total sugar content (%); C is the amount of sugar (μg) looked up from the standard curve that corresponded to the measured absorbance; D is dilution multiple; V_T is the total volume of the extract ($V_T = 100$ mL), V_S is the volume of the extract taken during measurement ($V_S = 1$ mL); W is the mass of the apple sample ($W = 1$ g).

In this study, 60 Fuji apple samples were randomly divided into correction set and prediction set at a ratio of 2:1. Table 2 lists the variation range, average value and standard deviation of the measured values of apple's total sugar content.

2.6 Data processing and analysis

All of the acquired spectral images were processed and analyzed by the ENVI 5.1 (Research System Inc., Boulder, CO., USA), Origin 2021 (Originlab, USA) and Matlab 2021a (The MathWorks Inc., Natick, USA) image processing toolbox.

Table 1. Preparation data of glucose solution in seven test tubes.

| Tube No. | 1 | 2 | 3 | 4 | 5 | 6 | 7 |
|--------------------------------|---|-----|-----|-----|-----|-----|-----|
| Glucose standard solution/mL | 0 | 0.1 | 0.2 | 0.3 | 0.4 | 0.6 | 0.8 |
| Distilled water/mL | 1 | 0.9 | 0.8 | 0.7 | 0.6 | 0.4 | 0.2 |
| Glucose content/ μg | 0 | 10 | 20 | 30 | 40 | 60 | 80 |

Table 2. Statistical results of total sugar content detection in correction set and prediction set of apple samples.

| Subset | Sample | Range/% | Mean/% | Standard deviation/% |
|-----------------|--------|------------|--------|----------------------|
| Calibration set | 40 | 7.14~11.72 | 9.25 | 1.1281 |
| Prediction set | 20 | 6.49~11.48 | 9.40 | 1.2075 |

The average spectrum of ROI is processed by continuum removal. continuum removal is a spectral analysis method that can effectively enhance the absorption characteristics of interest. It can effectively highlight the absorption and reflection characteristics of the spectral curve, normalize the reflectance to 0~1.0, and normalize the absorption characteristics of the spectrum to the consistent spectral background. It is conducive to comparing the characteristic values with other spectral curves, to extract the characteristic bands for classification and recognition.

2.7 Prediction model establishment for apple total sugar content

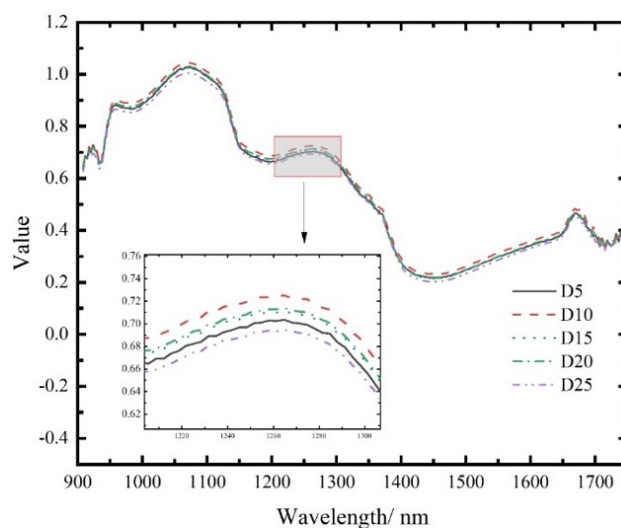
The quantitative analysis model of apples' total sugar content was established by the PLS method. PLS is an excellent multivariate statistical data analysis method, which can simultaneously realize regression modeling (multiple linear regression), data structure simplification (principal component analysis) and correlation analysis (canonical correlation analysis) between two groups of variables. By projecting the high-dimensional data space of the independent variable and the dependent variable into the corresponding low-dimensional space, the orthogonal eigenvectors of the independent variable and the dependent variable are obtained respectively, and then the univariate linear regression relationship between the eigenvectors of the independent variable and the dependent variable is established (Yang et al., 2022). It is suitable for the model building when the sample size is small. The model is comprehensively evaluated by the correlation coefficient R_c between the measured value and the predicted value of the correction set, the correlation coefficient R_p between the measured value and the predicted value of the prediction set, the root mean square error of calibration (RMSEC) and the root mean square error of prediction (RMSEP). In the process of establishing the PLS analysis model, the number of principal factors is determined by the minimum root mean square error. If the number of selected principal factors is too small, more useful information of the original spectrum will be lost and the fitting will be insufficient; if the number of selected principal factors is too large, too much noise will be absorbed, and the phenomenon of overfitting will appear, causing the prediction error of the established model significantly increasing.

3 Results

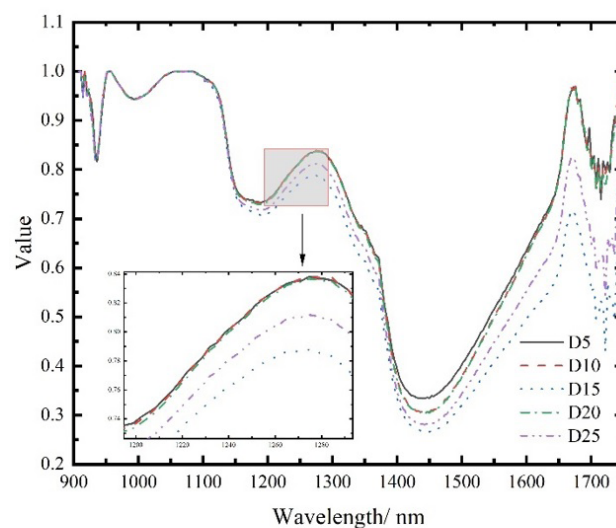
3.1 Analysis of spectral characteristics of ROI

The reflection spectra of different sizes square ROI and circular ROI in the effective band range of apple hyperspectral images are shown in Figure 2 and Figure 3 (corrected by black and white plate). It can be seen from the two figures that the five spectral curves are more discriminative after continuum removal; the overall trends of the reflectance spectra of the square ROI and the circular ROI are almost the same, and the overall trends of the reflectance spectra of different ROI are also basically the same.

The spectrum of ROI of the calibration set sample after black and white plate correction and continuum removal is shown in Figure 4. The noise at 900~950 nm and 1700~1750 nm is relatively large, and the signal-to-noise ratio is low; the obvious



(a) Before continuum removal



(b) After continuum removal

Figure 2. Comparison of average spectra of square ROI with different sizes.

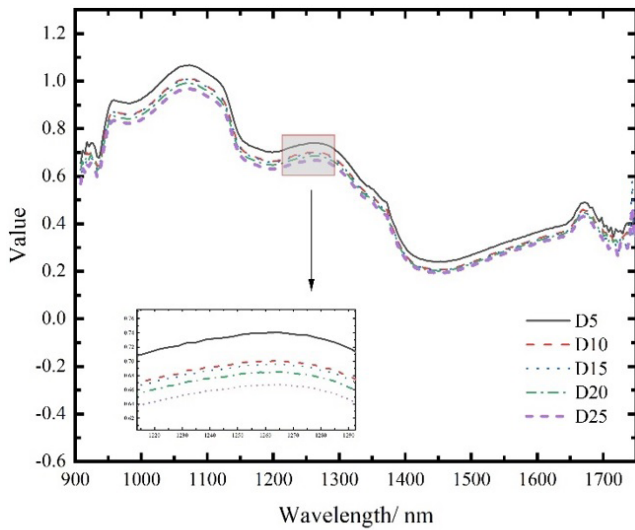
peaks are 1050 nm, 1280 nm, and 1680 nm, and the troughs are 1160 nm and 1430 nm. Considering the signal-to-noise ratio and saturation at both ends, the spectral data in the range of 1150~1650 nm was selected for the establishment of a quantitative analysis model for the sugar content of apples.

3.2 Prediction results based on the PLS model

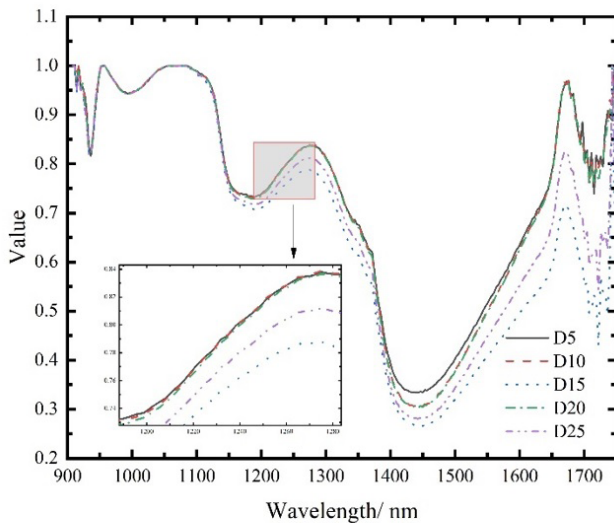
The PLS method was used to establish models for the spectral data of ROI with different shapes and sizes (Pranoto et al., 2022; Rambo et al., 2020), and the results are shown in Table 3. The correlation coefficient and RMSE of the calibration set and the prediction set were improved with the expansion of the selected area for the circular and square ROIs. The detection model established using a circular ROI with a radius of 25 pixels has the best results. The correlation coefficient and root mean square error of the calibration set are 0.8977 and 0.6459, and

Table 3. Comparison of apple total sugar content prediction results based on ROI with different sizes and shapes.

| Shape | Size | PLS factor | Calibration set | | Prediction set | |
|-----------|------|------------|-----------------|---------|----------------|---------|
| | | | R_c | RMSEC/% | R_p | RMSEP/% |
| Square | D5 | 5 | 0.8217 | 0.6701 | 0.7983 | 0.7108 |
| | D10 | 5 | 0.8706 | 0.6691 | 0.8201 | 0.7092 |
| | D15 | 5 | 0.8767 | 0.6504 | 0.8376 | 0.7009 |
| | D20 | 5 | 0.8614 | 0.6607 | 0.8401 | 0.6981 |
| | D25 | 5 | 0.8723 | 0.6518 | 0.8489 | 0.6796 |
| Roundness | D5 | 5 | 0.8731 | 0.6673 | 0.8506 | 0.6921 |
| | D10 | 5 | 0.8892 | 0.6509 | 0.8703 | 0.6743 |
| | D15 | 5 | 0.8879 | 0.6501 | 0.8517 | 0.6729 |
| | D20 | 5 | 0.8953 | 0.6476 | 0.8729 | 0.6641 |
| | D25 | 5 | 0.8977 | 0.6459 | 0.8836 | 0.6627 |



(a) Before continuum removal



(b) After continuum removal

Figure 3. Comparison of average spectra of circular ROI with different sizes.

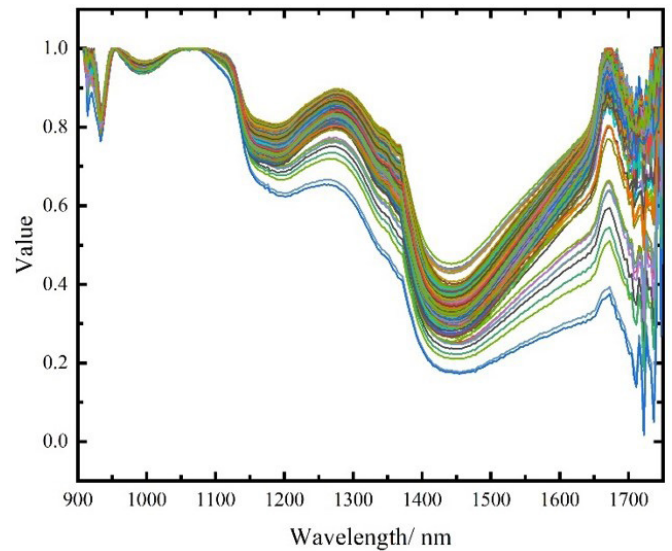


Figure 4. The apple spectrum of the calibration set.

the correlation coefficient and root mean square error of the prediction set are 0.8836 and 0.6627.

Figure 5 is the scatter plot between the predicted values and the measured values of the calibration set samples and the predicted set. It can be seen that the predicted values have a good correlation with the measured values, and shows that the hyperspectral image technology is effective for non-destructive testing of apple's total sugar content.

4 Discussion and conclusion

Apple is a spherical body, and the fruit shape is irregular, thus causing uneven light distribution on the surface, which will cause fluctuations in the average spectrum. Properly expanding the area of ROI and taking the average spectrum of the region has a certain homogenization effect on the spectral fluctuation phenomenon, and at the same time is conducive to eliminating

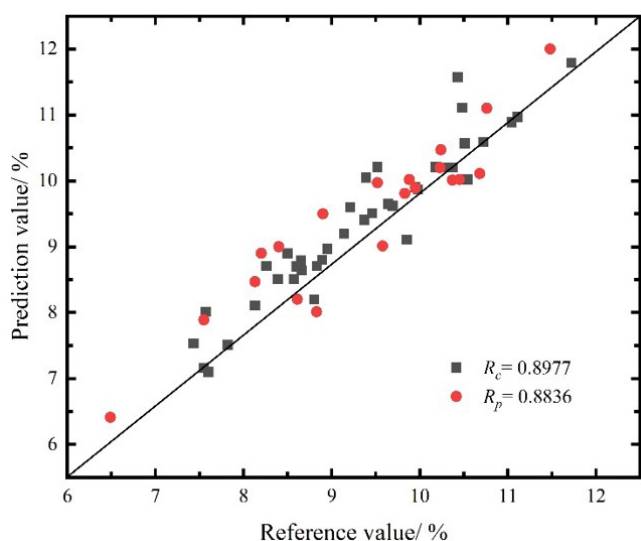


Figure 5. Scatter plots of the calibration set and prediction set based apple sugar content prediction model.

the random noise of each pixel, reducing the randomness of spectrum selection, and improving the stability and accuracy of the prediction model. In addition, using the continuum removal method to process the spectral signals is conducive to increasing the discrimination between the spectral signals of the samples, which is conducive to the detection of the total sugar content of apples.

The average spectra of circular and square ROI with different sizes are extracted from hyperspectral images, then the PLS method is used to establish the quantitative analysis model of the total sugar content of apples after continuum removal, and the prediction set of independent samples is used to verify the model. The influence of the shape and size of ROI on the modeling accuracy of hyperspectral images is analyzed. We found that the prediction result of the circular ROI with a radius of 25 pixels was the best, with the correlation coefficient R_c of the correction set being 0.8977, RMSEC being 0.6459, and the correlation coefficient R_p of the prediction set being 0.8836, and RMSEP being 0.6627. The research shows that selecting ROI with appropriate shape and size is of great significance to improve the model accuracy and give play to the technical advantages of hyperspectral images.

Ethical approval

This article does not contain any studies with human participants or animals performed by any of the authors.

Conflict of interest

The authors declare no conflict of interest.

Availability of data and material

The raw/processed data required to reproduce these findings cannot be shared at this time as the data also forms part of an ongoing study.

Funding

Supported by the National Natural Science Foundation of China (11964030) and the Open Project of Key Laboratory of Modern Agricultural Engineering in Colleges and Universities of the Department of Education of the Autonomous Region (TDNG2021201).

References

- Armoogum, V., & Boodhoo, K. (2020). Full optimization and validation of an HPLC method for the quantitative analysis of total sugars in a soft drink. *Bulletin of the Chemical Society of Ethiopia*, 34(2), 419-426. <http://dx.doi.org/10.4314/bcse.v34i2.17>.
- Bai, H. X., Xue, Q. S., Hao, X. J., Li, H., Huang, L. Y., Li, C., & Yang, J. Y. (2022). Underwater hyperspectral imaging system with dual-scanning mode. *Applied Optics*, 61(15), 4226-4237. <http://dx.doi.org/10.1364/AO.456363>.
- Cao, Q., Yu, G. L., Sun, S. J., Dou, Y., Li, H., & Qiao, Z. Y. (2022). Monitoring water quality of the Haihe River based on ground-based hyperspectral remote sensing. *Water*, 14(1), 22. <http://dx.doi.org/10.3390/w1401022>.
- Chang, D., Liu, H., An, M., Hong, D., Fan, H., Wang, K., & Li, Z. (2022). Integrated transcriptomic and metabolomic analysis of the mechanism of foliar application of hormone-type growth regulator in the improvement of grape (*Vitis vinifera* L.) coloration in saline-alkaline soil. *Plants*, 11(16), 2115. <http://dx.doi.org/10.3390/plants11162115>. PMID:36015418.
- Chen, M., Ni, Y. L., Jin, C. Q., Liu, Z., & Xu, J. S. (2022). Spectral inversion model of the crushing rate of soybean under mechanized harvesting. *Food Science and Technology*, 42, e123221. <http://dx.doi.org/10.1590/fst.123221>.
- Duan, P. H., Xie, Z. J., Kang, X. D., & Li, S. T. (2022). Self-supervised learning-based oil spill detection of hyperspectral images. *Science China. Technological Sciences*, 65(4), 793-801. <http://dx.doi.org/10.1007/s11431-021-1989-9>.
- Egorov, V. D., & Kozoderov, V. V. (2021). Identification of forest vegetation using airborne hyperspectral data. *Izvestiya. Atmospheric and Oceanic Physics*, 57(12), 1538-1548. <http://dx.doi.org/10.1134/S0001433821120288>.
- Fu, X. P., & Wang, M. Y. (2022). Detection of early bruises on pears using fluorescence hyperspectral imaging technique. *Food Analytical Methods*, 15(1), 115-123. <http://dx.doi.org/10.1007/s12161-021-02092-3>.
- Li, B., Yin, H., Liu, Y.-D., Zhang, F., Yang, A.-K., Su, C.-T., & Ou-Yang, A.-G. (2022a). Detection storage time of mild bruise's yellow peaches using the combined hyperspectral imaging and machine learning method. *Journal of Analytical Science and Technology*, 13(1), 24. <http://dx.doi.org/10.1186/s40543-022-00334-5>.
- Li, C. F., Liu, L., Zhao, J. J., & Liu, X. F. (2022b). LF-CNN: deep learning-guided small sample target detection for remote sensing classification. *Cmes-Computer Modeling in Engineering & Sciences*, 131(1), 429-444. <http://dx.doi.org/10.32604/cmes.2022.019202>.
- Liu, H., Yu, T., Hu, B., Hou, X., Zhang, Z., Liu, X., Liu, J., Wang, X., Zhong, J., Tan, Z., Xia, S., & Qian, B. (2021). UAV-borne hyperspectral imaging remote sensing system based on acousto-optic tunable filter for water quality monitoring. *Remote Sensing*, 13(20), 4069. <http://dx.doi.org/10.3390/rs13204069>.
- Miller, D. L., Wetherley, E. B., Roberts, D. A., Tague, C. L., & McFadden, J. P. (2022). Vegetation cover change during a multi-year drought in Los Angeles. *Urban Climate*, 43, 101157. <http://dx.doi.org/10.1016/j.uclim.2022.101157>.

- Mu, C., Yuan, Z., Ouyang, X., Sun, P., & Wang, B. (2021). Non-destructive detection of blueberry skin pigments and intrinsic fruit qualities based on deep learning. *Journal of the Science of Food and Agriculture*, 101(8), 3165-3175. <http://dx.doi.org/10.1002/jsfa.10945>. PMID:33211339.
- Paunović, S. M., Mašković, P., & Milinković, M. (2020). Determination of primary metabolites, vitamins and minerals in black mulberry (*Morus nigra*) berries depending on altitude. *Erwerbs-Obstbau*, 62(3), 355-360. <http://dx.doi.org/10.1007/s10341-020-00509-7>.
- Pi, W., Du, J., Bi, Y., Gao, X., & Zhu, X. (2021). 3D-CNN based UAV hyperspectral imagery for grassland degradation indicator ground object classification research. *Ecological Informatics*, 62, 101278. <http://dx.doi.org/10.1016/j.ecoinf.2021.101278>.
- Pranoto, W. J., Al-Shawi, S. G., Chetthamrongchai, P., Chen, T. C., Petukhova, E., Nikolaeva, N., Abdelbasset, W. K., Yushchenko, N. A., & Aravindhana, S. (2022). Employing artificial neural networks and fluorescence spectrum for food vegetable oils identification. *Food Science and Technology*, 42, e80921. <http://dx.doi.org/10.1590/fst.80921>.
- Rambo, M. K. D., Ferreira, M. M. C., Melo, P. M., Santana, C. C. Jr., Bertuol, D. A., & Rambo, M. C. D. (2020). Prediction of quality parameters of food residues using NIR spectroscopy and PLS models based on proximate analysis. *Food Science and Technology*, 40(2), 444-450. <http://dx.doi.org/10.1590/fst.02119>.
- Saafi, E. B., Arem, A., Chahdoura, H., Flamini, G., Lachheb, B., Ferchichi, A., Hammami, M., & Achour, L. (2022). Nutritional properties, aromatic compounds and in vitro antioxidant activity of ten date palm fruit (*Phoenix dactylifera* L.) varieties grown in Tunisia. *Brazilian Journal of Pharmaceutical Sciences*, 58, e18871. <http://dx.doi.org/10.1590/s2175-97902020000318871>.
- Sulaiman, N., Che'Ya, N. N., Roslim, M. H. M., Juraimi, A. S., Noor, N. M., & Ilahi, W. F. F. (2022). The application of Hyperspectral Remote Sensing Imagery (HRSI) for weed detection analysis in rice fields: a review. *Applied Sciences*, 12(5), 2570. <http://dx.doi.org/10.3390/app12052570>.
- Sun, X., Liu, J. J., Sun, J. F., Zhang, H., Guo, Y. M., Zhao, W. P., Xia, L., & Wang, B. (2021). Visual detection of moldy peanut kernels based on the combination of hyperspectral imaging technology and chemometrics. *Journal of Food Process Engineering*, 44(11), e13864. <http://dx.doi.org/10.1111/jfpe.13864>.
- Wang, T. T., Li, G. H., & Dai, C. L. (2022). Soluble solids content prediction for Korla fragrant pears using hyperspectral imaging and GsMIA. *Infrared Physics & Technology*, 123, 104119. <http://dx.doi.org/10.1016/j.infrared.2022.104119>.
- Xu, M., Sun, J., Yao, K. S., Wu, X. H., Shen, J. F., Cao, Y., & Zhou, X. (2022). Nondestructive detection of total soluble solids in grapes using VMD-RC and hyperspectral imaging. *Journal of Food Science*, 87(1), 326-338. <http://dx.doi.org/10.1111/1750-3841.16004>. PMID:34940982.
- Yang, S., Zhang, H. Q., & Fan, W. M. (2022). Characteristic wavelengths selection of rice spectrum based on adaptive sliding window permutation entropy. *Food Science and Technology*, 42, e38922. <http://dx.doi.org/10.1590/fst.38922>.
- Ye, C., Li, H., Li, C., Liu, X., Li, Y., Li, J., Gonçalves, W. N., & Marcato, J. Jr. (2021). A building roof identification CNN based on interior-edge-adjacency features using hyperspectral imagery. *Remote Sensing*, 13(15), 2927. <http://dx.doi.org/10.3390/rs13152927>.
- Yuan, R.-R., Wang, B., Liu, G.-S., He, J.-G., Wan, G.-L., Fan, N.-Y., Li, Y., & Sun, Y.-R. (2021). Study on the detection and discrimination of damaged jujube based on hyperspectral data. *Guangpuxue Yu Guangpu Fenxi*, 41(9), 2879-2885.
- Zhou, Z., Zhao, B., Wang, W., Tong, X., Zheng, J., Li, Y., Gao, J., Luo, F., Sun, S., & Pei, Z. (2022). Determination of three soluble sugars in stem juice of sweet sorghum by anthrone colorimetry. *Caoye Kexue*, 39(5), 940-948.
- Zou, Z. Y., Chen, J., Zhou, M., Zhao, Y. P., Long, T., Wu, Q. S., & Xu, L. J. (2022). Prediction of peanut seed vigor based on hyperspectral images. *Food Science and Technology*, 42, e32822. <http://dx.doi.org/10.1590/fst.32822>.